

Polariton-mediated binding of anti-aligned dipolar excitons

Haifeng Kang¹, Quanbing Guo^{1,2*}, Tianyi Zhou², Shun Feng³, Wei Dai^{1,2}, Kenji Watanabe⁴, Takashi Taniguchi⁵, Hongxing Xu^{1,2}, Ting Yu^{1,2*}, Xiaoze Liu^{1,2,6*}

¹ Key Laboratory of Artificial Micro/Nano Structure of Ministry of Education, School of Physics and Technology, Wuhan University, Wuhan, P. R. China

² Wuhan Institute of Quantum Technology, Wuhan, P. R. China

³ Institute of Electrical and Microengineering, École Polytechnique Fédérale de Lausanne (EPFL), Lausanne, Switzerland

⁴ Research Center for Functional Materials, National Institute for Materials Science, Ibaraki, Japan

⁵ International Center for Materials Anorthite, National Institute for Materials Science, Ibaraki, Japan

⁶ Wuhan National High Magnetic Field Center, Huazhong University of Science & Technology, Wuhan, 430074, P. R. China

Abstract

Interacting bosonic quasiparticles are the cornerstone for exploring many-body physics and nonlinear quantum phenomena in correlated light-matter systems. Strongly interacting dipolar excitons in van der Waals heterostructures have attracted significant interest due to their out-of-plane electric dipole moments and high tunability via the quantum-confined Stark effect (QCSE). However, leveraging these tunable dipolar excitons in strongly coupled exciton-photon systems to explore exotic many-body physics and macroscopic quantum phenomena remains experimentally elusive. Here, we report the strong coupling of dipolar excitons in a gated bilayer MoS₂ device integrated with a one-dimensional photonic crystal hosting bound-states-in-continuum (BIC). The resulting polaritons hybridize cavity photons with a coherent superposition of two electrically tunable anti-aligned dipolar excitons, effectively binding them into composite quasiparticle states. By tuning the dipolar excitons into non-degenerate states via the QCSE, we realize *in situ* reconfiguration of the polariton wavefunction and observe an emergent polariton branch exhibiting non-monotonic Stark shifts. Notably, these tunable polaritons allow for customized control over nonlinear interactions through distinct excitonic hybridization and dipolar configurations. This *in situ* tunability offers a scalable pathway toward electrically programmable quantum fluids of light and correlated polariton phases in on-chip photonic integrated circuits.

Introduction

Interacting photons are a central resource for quantum optics and nonlinear information processing^{1,2}. Through strong light–matter coupling in semiconductor cavities, exciton polaritons offer a practical route by combining photonic coherence and transport with exciton-mediated nonlinear interactions^{2–6}. These key features have enabled diverse macroscopic quantum phenomena rooted in Bose-Einstein condensation^{7,8}, and underpin promising on-chip photonic applications^{9–13} and quantum simulations^{14,15}. Although strategies such as artificial lattice potentials and charged exciton complexes have been employed to strengthen polariton interactions^{16–21}, the short-range nature of excitonic exchange interactions remains a recurring bottleneck. Dipolar excitons can surmount this limitation via dipolar interactions arising from their out-of-plane (OP) static electric dipole moments. While such capability has been successfully demonstrated with versatile tunability in conventional quantum well systems^{22–24}, van der Waals (vdW) semiconductors offer a compelling platform^{25–34}. Owing to their discrete layered structure, vdW heterostructures host interlayer excitons (IX) with layer-addressable out-of-plane (OP) dipole moments^{26,28–30,34}, enabling the precise engineering of dipolar interactions. However, they typically face a fundamental trade-off between oscillator strength and interaction strength^{25–34}, impeding the formation of strongly interacting dipolar polaritons in the strong coupling regime.

Naturally stacked 2H-bilayer MoS₂ (2L-MoS₂) overcomes this trade-off via tunneling-mediated hybrid IX of dipolar excitons. Facilitated by interlayer hole tunneling, the hybrid IX inherit substantial oscillator strength from intralayer excitons while maintaining strong dipolar interactions with OP dipole moments^{35–42}. Consequently, the IX in 2L-MoS₂ can achieve strong coupling with cavity photons, forming dipolar polaritons with significantly enhanced nonlinear interactions^{43–45}. Crucially, the hybrid IX consist of two degenerate dipolar states with anti-aligned OP dipole moments, capable of simultaneously supporting repulsive and attractive interactions⁴⁰ for exploring rich many-body physics^{35–42,46}. An applied vertical electric field (E_z) lifts this degeneracy via the quantum-confined Stark effect (QCSE)^{35–42,46}, resulting in two anti-aligned dipolar states characterized by split resonances and reduced oscillator strengths. This dipolar configuration enables on-demand programmability of the anti-aligned dipolar states and their polaritonic interactions. This capability is largely inaccessible to conventional quantum well systems^{22–24}, and has not yet been experimentally demonstrated.

In this context, we leverage the hybrid dipolar IX to demonstrate electrically

tunable dipolar polaritons in a gated 2L-MoS₂ device integrated with a one-dimensional photonic crystal (1DPC) hosting bound states in continuum (BIC). In the strong coupling regime, the resulting polaritons hybridize cavity photons with a coherent superposition of two anti-aligned dipolar excitons, effectively binding them into composite quasiparticle states. By applying an E_z -field via the QCSE, we lift the IX degeneracy into two distinct anti-aligned dipolar states with split resonances. This enables electrical reconfiguration of the polariton wavefunction via tunable IX hybridization, leading to the emergence of a new polariton branch. The new branch effectively binds these non-degenerate dipolar excitons and exhibits non-monotonic Stark shifts driven by the evolving IX composition. This reconfiguration of dipolar polaritons grants the *in situ* tunability of nonlinear bosonic interactions across different polariton branches. Ultimately, the ability to reconfigure the polariton wavefunction via tunable dipolar IX provides a pathway toward electrically programmable quantum fluids of light and exotic correlated polariton phases.

Results and discussions

Characterization of the hybrid 2L-MoS₂ system

We developed a hybrid architecture integrating a gated 2L-MoS₂ device with a 1DPC for this work, achieving strong coupling between the IX and photonic modes (Fig. 1a; see Methods and Supplementary Notes 1-2 for details). The gating device functions as a planar capacitor, consisting of a bilayer MoS₂ encapsulated by an insulator of few-layer hexagonal boron nitride (hBN), and contacted by two few-layer graphene electrodes. This configuration allows for the application of a tunable perpendicular electrostatic E_z -field to the 2L-MoS₂ to induce the QCSE of dipolar excitons. The gated device is fabricated atop the 1DPC, which features a Si₃N₄ grating structure with a period of 365 nm, a height of 106 nm, and a filling factor of 0.65 (see Methods and Supplementary Note 1 for details). The 1DPC hosts BIC with an extremely high quality factor (Q-factor) at the Γ point⁴⁷. Crucially, the 1DPC photonic modes exhibit a highly confined electromagnetic field near the interface between Si₃N₄ grating and the gating device, facilitating the strong coupling between the 1DPC and 2L-MoS₂ (see Supplementary Notes 1 and 3, Supplementary Figs. 1-2 for simulation details). With the fabricated samples, Fig. 1b shows a typical microscopic image. The lateral dimension of the exfoliated 2L-MoS₂ flake is ~ 40 μm , while the hBN and graphene extend to ~ 80 μm , ensuring optimal conditions for optical characterization and electrical control. A portion of the 2L-MoS₂ flake extends beyond the 1DPC region; this uncoupled area serves as a reference for accurately monitoring the intrinsic tunable exciton resonances.

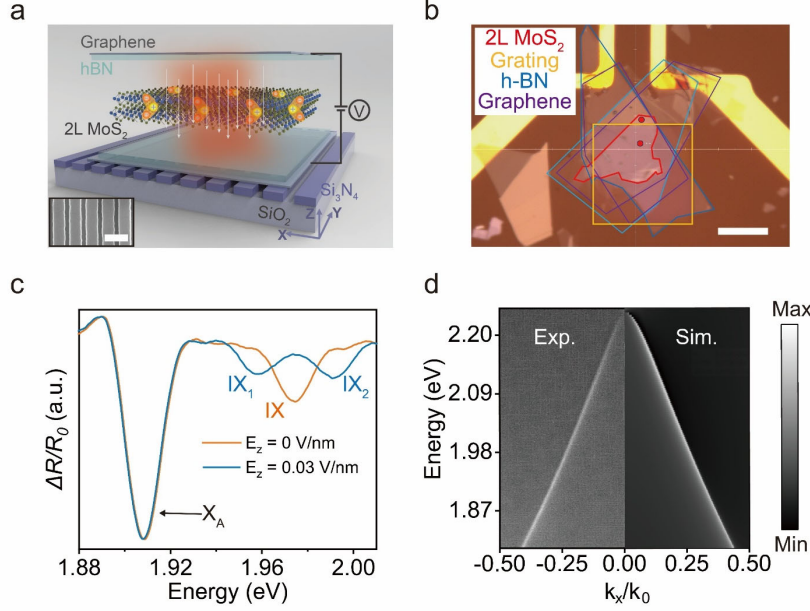


Fig. 1. Hybrid 2L-MoS₂ system for the tunable dipolar polaritons. (a) Schematics of a gated 2L-MoS₂ device on a Si₃N₄ grating-based 1DPC. The hybrid dipolar IX in 2L-MoS₂ strongly couple with the 1DPC photonic modes and can be controlled by the applied E_z -field. The inset shows the SEM image of 1DPC with a scale bar of 500 nm. (b) Optical microscopic image of one hybrid 2L-MoS₂ sample. The orange square outlines the area of the 1DPC. The red, blue, and purple lines mark the boundaries of 2L-MoS₂, few-layer hBN, and graphene, respectively. The two red dots represent the area on/off the 1DPC. The scale bar is 30 μ m. (c) The reflectance contrast spectra of 2L-MoS₂ with/without an applied E_z -field at 6 K. The hybrid IX is split into IX₁ and IX₂ with an E_z -field. (d) The experimental (left) and simulated (right) photonic dispersions of the 1DPC under TE polarization exhibit excellent agreement.

We then characterized the exciton resonances of the bare 2L-MoS₂ and the photonic resonances of the 1DPC. Figure 1c plots the reflectance contrast spectra of bare 2L-MoS₂ with/without an applied E_z -field. In the bare 2L-MoS₂ without E_z -field, we identify the main exciton resonance ~ 1.907 eV as A exciton (X_A) and the resonance at 1.974 eV as the hybrid IX (Fig. 1a, see Supplementary Note 2 and Supplementary Fig. 3)³⁶. In 2L-MoS₂, the IX feature localized electrons in one layer and delocalized holes across the bilayer, exhibiting degenerate dipolar states with anti-aligned OP dipole moments ($p_z = \pm e \cdot d$) and possess considerable oscillator strengths^{36,37,48}. Under an applied E_z -field, the QCSE lifts the dipolar IX degeneracy into two split resonances (IX₁ and IX₂) as $E_{IX_1} = E_{IX} - E_z \cdot p_z$ and $E_{IX_2} = E_{IX} + E_z \cdot p_z$, where E_{IX} , E_{IX_1} and E_{IX_2} represent the exciton resonances of IX, IX₁, and IX₂, respectively (Supplementary Fig. 4, and Supplementary Note 8)^{36,37,48}. For example, at an E_z -field of 0.03 V/nm, the resonances of IX₁ and IX₂ are well resolved

(Fig. 1c). In contrast, the QCSE is negligible for X_A , as they do not possess any OP dipole moments. Figure 1d displays the experimental and simulated photonic dispersions of the 1DPC under transverse-electric (TE) polarization (see Methods, Supplementary Note 1 and 3 for more details), which are in close agreement. The broad spectral range and tight confinements of the photonic modes (with a BIC mode ~ 2.24 eV at Γ point) enable the efficient coupling with all the excitons of interest in 2L-MoS₂.

Strong coupling regime and electrical tunability

We performed angle-resolved (k -space) reflectance spectroscopy to characterize the strong coupling regime and electrical tunability on the hybrid integrated sample of 2L-MoS₂ and 1DPC under different conditions. Figure 2a shows k_x -resolved reflectance spectra of the sample without the E_z -field. Pronounced anti-crossing features are observed in the vicinity of the IX and X_A resonances, indicating the formation of multiple polariton branches by the strong coupling between different excitons and the shared photonic mode. Here, we focus on the polariton branches associated with strong coupling to the IX, while a detailed discussion of coupling involving other excitons (e.g., X_A) is provided in Supplementary Note 4 and Supplementary Fig. 6. Intriguingly, upon applying an E_z -field ($E_z = 0.035$ V/nm), the feature of two polariton branches in the strong coupling regime of the sole IX evolves into two anti-crossing features with two energy-split excitons, leading to three polariton branches with an emergent middle branch (Fig. 2b). This indicates that the photonic mode now strongly couples with two emergent IX under the applied E_z -field, i.e., the QCSE induced IX₁ and IX₂. As the E_z -field increases ($E_z = 0.05$ V/nm), the three polariton branches are separated further, as expected for the strong coupling with more split resonance energies of IX₁ and IX₂ (Fig. 2c). This suggests the strong coupling with IX₁ and IX₂ persists even though these two excitons are further apart with increased E_z -field. Here, we label the polariton branches as lower, middle, and upper branches (LPB, MPB, UPB) based on their energies, as shown in Fig. 2b and 2c.

We employed a two-coupled-oscillator model to analyze the polariton Hamiltonian in the absence of E_z -field as (Supplementary Note 4)¹⁶:

$$H = \begin{pmatrix} E_{\text{ph}} - i\gamma_{\text{ph}}/2 & V \\ V & E_{\text{IX}} - i\gamma_{\text{IX}}/2 \end{pmatrix} \quad (1)$$

where E_{ph} and γ_{ph} represent the energy and linewidths of the photonic mode, γ_{IX} represents the IX linewidth, V denotes the exciton-photon coupling strength. By fitting the experimentally extracted polariton resonances (the dashed rectangular area in Fig. 2a), we determine Rabi splitting $\hbar\Omega_{\text{IX}} = \sqrt{4V^2 - (\gamma_{\text{ph}} - \gamma_{\text{IX}})^2} = 38.06 \pm 0.16 \text{ meV}$ between the LPB and UPB as shown in Fig. 2d. When the IX_1 and IX_2 emerge via the QCSE, we analyzed the polariton Hamiltonian via a three-coupled-oscillator model as (Supplementary Notes 3-5, Supplementary Fig. 5)¹⁶:

$$H = \begin{pmatrix} E_{\text{ph}} - \frac{i\gamma_{\text{ph}}}{2} & V_{\text{IX}_1} & V_{\text{IX}_2} \\ V_{\text{IX}_1} & E_{\text{IX}_1} - \frac{i\gamma_{\text{IX}_1}}{2} & 0 \\ V_{\text{IX}_2} & 0 & E_{\text{IX}_2} - \frac{i\gamma_{\text{IX}_2}}{2} \end{pmatrix} \quad (2)$$

where γ_{IX_1} and γ_{IX_2} represent IX_1 and IX_2 linewidths, V_{IX_1} and V_{IX_2} denote the coupling strengths for IX_1 and IX_2 , respectively. Similarly, in Fig. 2e, f, we determine the Rabi splittings by fitting the polariton resonances (the rectangular areas in Figs. 2b and 2c) as: $\hbar\Omega_{\text{IX}_1} = 30.58 \pm 0.56 \text{ meV}$, $\hbar\Omega_{\text{IX}_2} = 19.25 \pm 0.56 \text{ meV}$ at $E_z = 0.035 \text{ V/nm}$; $\hbar\Omega_{\text{IX}_1} = 27.48 \pm 0.56 \text{ meV}$, $\hbar\Omega_{\text{IX}_2} = 30.96 \pm 0.56 \text{ meV}$ at $E_z = 0.050 \text{ V/nm}$. Clearly, all the Rabi splittings always satisfy the strong coupling criterion $(\hbar\Omega)^2 > (\gamma_{\text{ph}}^2 + \gamma_{\text{IX}}^2)/4$, verifying the robust strong coupling regime in all the cases. We reproduced these results in an independent device (Supplementary Fig. 14), demonstrating the robustness and reproducibility of the strong coupling regime and electrical control.

Notably, both $\hbar\Omega_{\text{IX}_1}$ and $\hbar\Omega_{\text{IX}_2}$ are smaller than the zero-field $\hbar\Omega_{\text{IX}}$ as the E_z -field increases. Since the Rabi splitting $\hbar\Omega$ is proportional to the square root of the oscillator strength ($\Omega \propto \sqrt{f}$), this reduction indicates that the oscillator strength of the original IX resonance is distributed between the anti-aligned IX_1 and IX_2 states. This behavior is consistent with the QCSE: the initially degenerate IX splits into two non-degenerate IX_1 and IX_2 , effectively decomposing the IX oscillator strength (f_{IX}) into f_{IX_1} and f_{IX_2} . Moreover, the extracted $\hbar\Omega_{\text{IX}_1}$ and $\hbar\Omega_{\text{IX}_2}$ exhibit a trade-off as the E_z -field is tuned. This is likely attributed to the opposing E_z -field dependences of the anti-aligned dipolar excitons, where the IX_1 becomes more polarized by the QCSE accompanied by a decrease in energy and f_{IX_1} while the IX_2 exhibits the converse behavior. We also analyzed the strong coupling involving X_A and the

corresponding polaritons, which remain essentially insensitive to the applied E_z -field (Supplementary Note 4 and Supplementary Fig. 6).

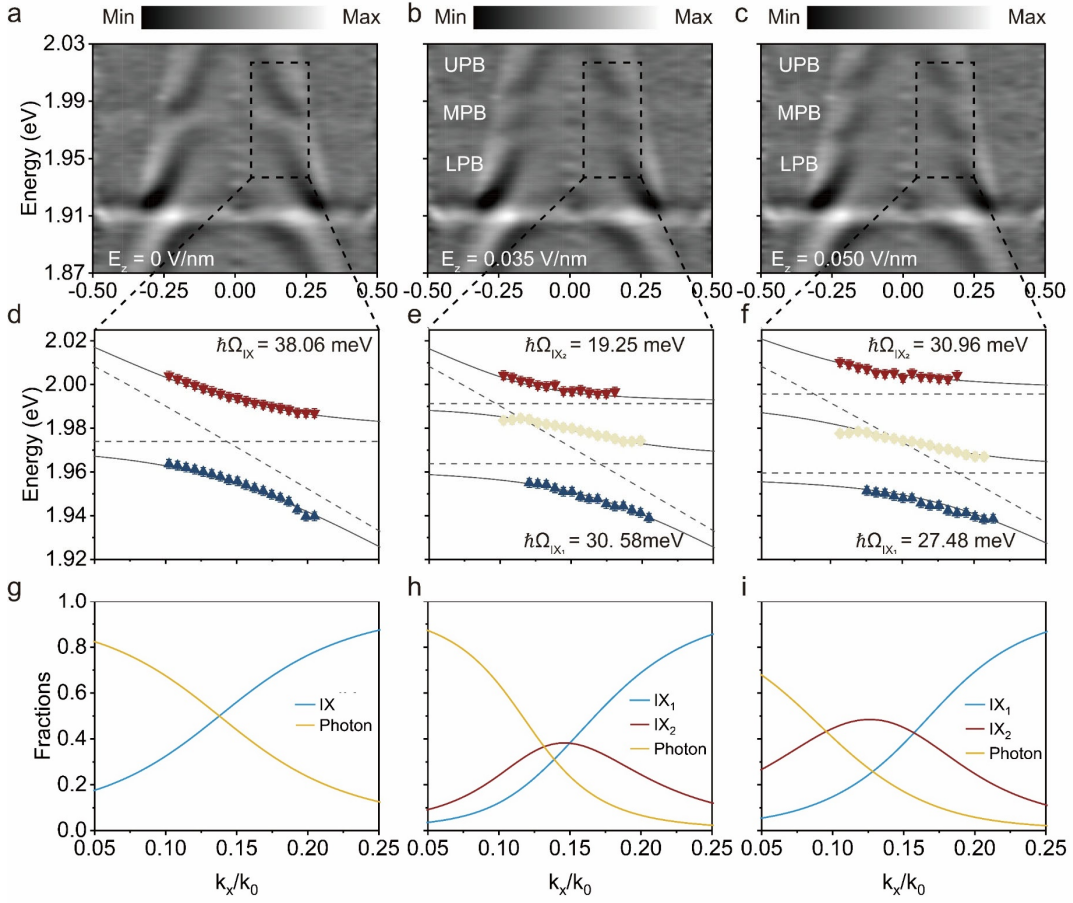


Fig. 2. Tunable strong coupling regime via the QCSE. Angle-resolved (k_x -resolved) reflectance spectra (a) at zero E_z -field, (b) at $E_z = 0.035$ V/nm, and (c) at $E_z = 0.050$ V/nm. (d-f) Extracted polariton energies (data points) in the zoomed-in rectangular regions from (a-c) and fitted polariton dispersions (solid curves). Note that the dashed lines denote the uncoupled photonic modes and excitonic resonances. (g-i) The constituent fractions derived from Hopfield coefficients (g) at zero E_z -field, (h) at $E_z = 0.035$ V/nm, and (i) at $E_z = 0.050$ V/nm.

Leveraging the coupled-oscillator model, we elucidate the field-tunable correlation in the hybridization of anti-aligned dipolar excitons within the strong coupling regime. Figures 2g-i display the corresponding exciton and photon fractions of LPB at zero E_z -field and MPB at $E_z = 0.035$ V/nm, 0.050 V/nm. At zero E_z -field, the polariton branches are the hybridization of the degenerate IX resonance and cavity photons. Upon the application of the E_z -field, however, all polariton branches evolve into hybrid states composed of photons and both anti-aligned dipolar excitons with field-dependent weighting. While the LPB (UPB) is dominated by the

hybridization of IX_1 (IX_2) and photons (Supplementary Fig. 9), the emergent MPB exhibits a distinct character, primarily composed of a coherent superposition of both IX_1 and IX_2 . Crucially, this distinct MPB effectively mediates the binding of two anti-aligned dipolar excitons into a single composite quasiparticle, as detailed below.

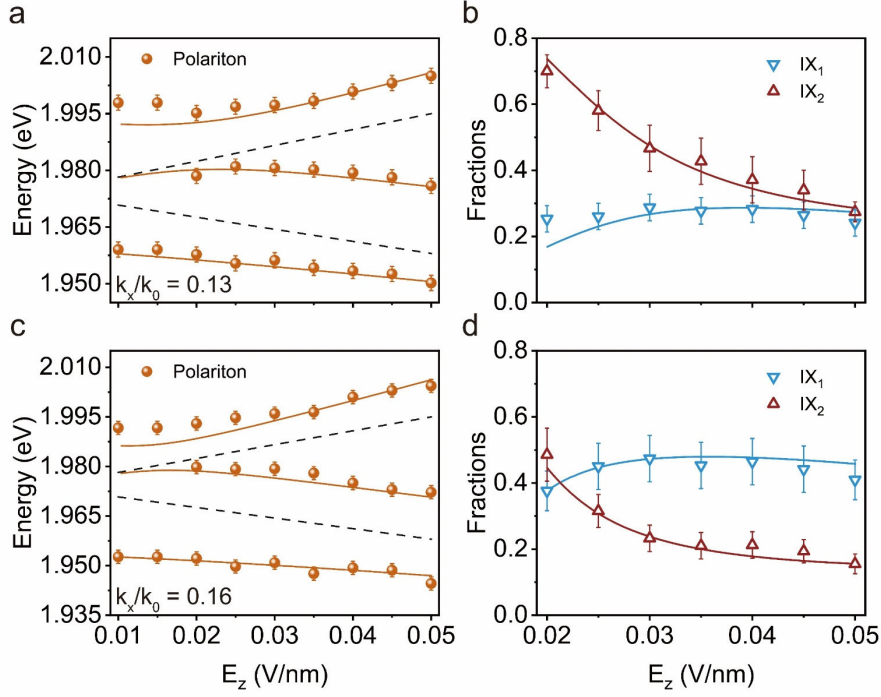


Fig. 3. Tunable hybridization of dipolar excitons. Extracted polariton energies (colored data points) and uncoupled dipolar exciton energies (dashed lines) as a function of the E_z -field for the spectra at (a) $k_x/k_0 = 0.13$ and (c) $k_x/k_0 = 0.16$. The solid lines denote the calculated polariton energies with the E_z -field-dependent coupled-oscillator model. The excitonic fractions of MPB based on the experimental data (discrete points) and the predicted fractions from the E_z -field-dependent coupled-oscillator model for (b) $k_x/k_0 = 0.13$ and (d) $k_x/k_0 = 0.16$.

To elucidate the E_z -field-dependent hybridization of the dipolar excitons, we analyze the polaritons at two typical in-plane momenta ($k_x/k_0 = 0.13$ and 0.16) with E_z -field-dependent coupled-oscillator model. Figures 3a and 3c respectively plot the extracted polariton energies at the two momenta, as the E_z -field is continuously varied. For reference, we also overlay the field-dependent dipolar energies (dashed lines) of non-degenerate, anti-aligned IX_1 and IX_2 based on their linear Stark trends of the uncoupled 2L-MoS₂ region (Supplementary Note 5 and Supplementary Fig. 7). Correspondingly, although the detailed E_z -field dependence differs at the two momenta, the polaritonic spectrum in both cases evolves from two branches (UPB and LPB) to three branches (UPB, MPB, and LPB). The UPB (LPB) exhibits

monotonic blueshifts (redshifts), reflecting the dominant contribution from the blue-shifted IX_2 (red-shifted IX_1) induced by the QCSE. Crucially, MPB resides energetically between IX_1 and IX_2 states and exhibits non-monotonic Stark shifts, arising from a distinct superposition state that effectively binds both anti-aligned dipolar excitons.

We further interpret the distinctive hybridization of these polariton branches using an E_z -field-dependent coupled-oscillator model. For each value of E_z , the excitonic fractions (from the Hopfield coefficients) are obtained by fitting the calculated polariton energies to the experimentally extracted data, as shown by the solid curves in Figs. 3a and 3c (see Supplementary Note 5 and Supplementary Fig. 8 for details). The resulting IX_1 and IX_2 excitonic fractions of the MPB are plotted in Figs. 3b and 3d, and consistent with the experimentally extracted fractions (overlaid scatter points). Here, we focus on the hybridization of the anti-aligned dipolar excitons; the associated field-dependent photon fractions are presented in Supplementary Fig. 10. Specifically at $k_x/k_0 = 0.13$, the exciton fractions of the IX_1 and IX_2 in the MPB are strongly imbalanced at small E_z -field but are more balanced at large E_z -field. On the contrary, at $k_x/k_0 = 0.16$, the exciton fractions of IX_1 and IX_2 are almost balanced at small E_z -field but become increasingly imbalanced at large E_z -field. Despite these momentum-dependent variations, the MPB consistently hybridizes photons with a coherent superposition of the anti-aligned, non-degenerate IX_1 and IX_2 . Consequently, the MPB effectively bind both anti-aligned IX with field-tunable hybridization weights that can be widely and reversibly reconfigured by the QCSE, resulting in non-monotonic Stark shifts. As the E_z -field increases, the MPB at $k_x/k_0 = 0.13$ initially exhibits a slight blueshift due to the dominant contribution of the blue-shifted IX_2 , eventually returning to zero-field energy as the contributions from the two IX become balanced. Conversely, at $k_x/k_0 = 0.16$, the MPB initially displays a negligible Stark shift due to balanced IX contributions, but subsequently undergoes a redshift as the IX_1 contribution becomes dominant.

Polariton nonlinearity controlled by tunable hybridization of dipolar excitons

By exploiting the electrically tunable hybridization of dipolar excitons, we investigated polariton nonlinearity using power-dependent spectroscopy and examined how the nonlinear response correlates with the constituents. Specifically, we analyze the power-dependent reflectance spectral shifts of representative polariton branches (i.e., LPB-X_A, LPB-IX, LPB-IX₁, UPB-IX₂, MPB) at selected k_x/k_0 and E_z -fields to disentangle nonlinear contributions associated with dominant X_A, IX, IX₁, and IX₂ constituents (See details in Supplementary Note 6 and Supplementary Figs.

11-12). As the polariton density increases, LPB-X_A (with a dominant X_A fraction of 0.5) exhibits slight blueshifts regardless of the applied E_z -field (Fig. 4a and Supplementary Fig. 11), which is similar to previous report¹⁶. However, the LPB-IX (with a dominant IX fraction of 0.5) undergoes apparent blueshifts and exhibits significantly stronger nonlinearity than LPB-X_A (Fig. 4b). When $E_z = 0.025$ V/nm is applied, LPB-IX₁ (with a dominant IX₁ fraction of 0.6) and UPB-IX₂ (with a dominant IX₂ fraction of 0.5) show apparent blueshifts and redshifts, respectively, demonstrating a convergence trend towards the IX₁ and IX₂ states (Fig. 4c). Intriguingly, we observe complex saturation-like redshifts for the MPB (characterized by IX₁ and IX₂ fractions of 0.2, 0.5, respectively), signaling unique nonlinear interactions via the dipolar exciton hybridization.

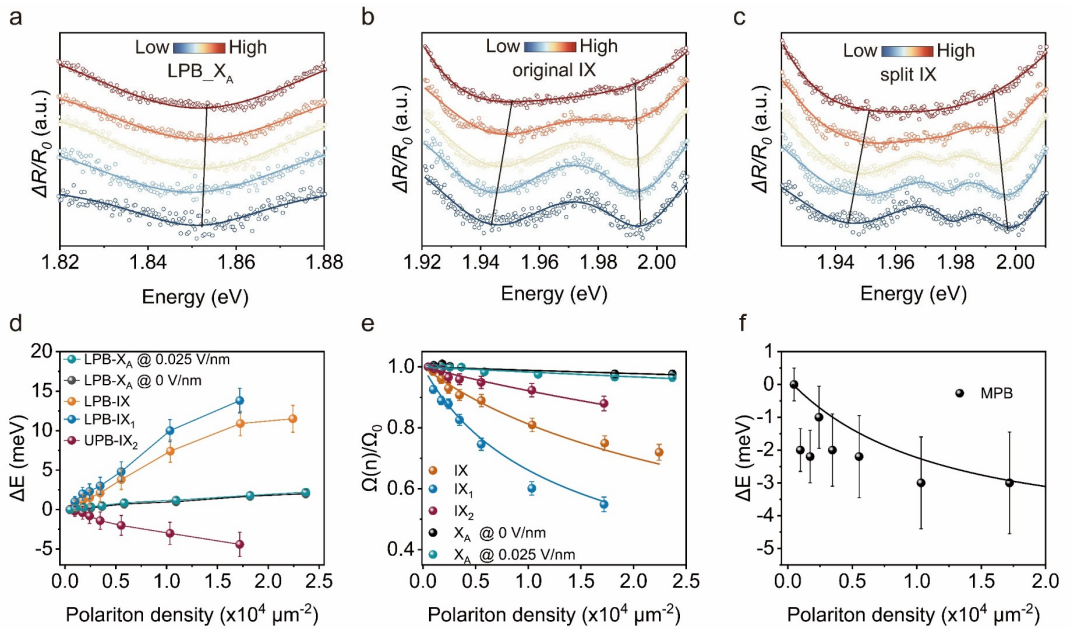


Fig. 4. Distinct polariton nonlinearity and quantitative analysis. Reflectance contrast spectra of (a) around LPB-X_A at zero E_z -field, (b) around IX at zero E_z -field, and (c) around IX₁ and IX₂ at $E_z = 0.025$ V/nm as a function of pump fluence. Solid lines in (a-c) are fitting results by the Lorentzian model. Summarized (d) energy shifts for representative polariton branches, (e) Rabi splittings, and (f) MPB energy shifts as a function of the polariton density. The solid lines in (e) are theoretical fits, and the solid curve in (f) is the calculated energy shift.

To quantitatively assess the exciton-dependent polariton nonlinearity, we extract the density-induced energy shifts of the selected branches (Fig. 4d) and compare them with the power-dependent Rabi splittings (Fig. 4e). The summarized shifts in Fig. 4d indicate that the polariton interaction strength is weakest for the LPB-X_A, significantly enhanced for the LPB-IX, and strongest for the LPB-IX₁. In contrast, the LPB-IX₂ exhibits a moderate interaction strength with the opposite sign (see

Supplementary Note 6 and Supplementary Fig. 11-13 for more details). By analyzing the polariton hybridization and power-dependent Rabi splittings (Fig. 4e), we find that the polariton nonlinearity in all these representative branches arises primarily from the phase-space filling (PSF) effect. Generally, polariton nonlinearity originates from two mechanisms: PSF-induced saturation and excitonic interactions. To quantify the PSF contribution, we extracted the power-dependent Rabi splitting for X_A , IX, IX_1 , and IX_2 (Fig. 4e). The X_A Rabi splitting exhibits only a minor reduction, consistent with the tiny spectral blueshifts for LPB- X_A . In contrast, the IX Rabi splitting shows a pronounced attenuation with increasing density. Moreover, the attenuation occurs more rapidly for IX_1 compared to IX_2 , revealing distinct saturation behaviors. These trends and the energy shifts are in good agreement with the branch-dependent spectral shifts discussed above, suggesting the polariton nonlinearity is dominated by the reduction of Rabi splitting via PSF effect. Furthermore, we estimated the expected energy shifts based on the exciton fractions of each polariton branch and bare exciton interactions⁴⁰, which are significantly smaller than the observed polariton energy shifts. This confirms that the polariton nonlinearity predominantly stems from the PSF effect.

To elaborate on the PSF effect, we adopt a simplified model commonly used to describe PSF-induced saturation¹⁶ as $\Omega(n) = \frac{\Omega_0}{\sqrt{1 + \frac{n}{n_s}}}$, where n_s denotes the saturation density. We extracted the saturation densities for X_A , IX, IX_1 , and IX_2 , which are respectively $4.43 \times 10^5 \mu\text{m}^{-2}$ ($3.01 \times 10^5 \mu\text{m}^{-2}$ at $E_z = 0.025 \text{ V/nm}$), $1.94 \times 10^4 \mu\text{m}^{-2}$, $7.76 \times 10^3 \mu\text{m}^{-2}$, and $5.56 \times 10^4 \mu\text{m}^{-2}$. While the saturation density of X_A is much higher than that of IX, IX_1 , and IX_2 . The difference between IX_1 and IX_2 likely originates from the QCSE-modified dipolar exciton wavefunctions⁴¹. Particularly, the applied E_z -field enhances the IX spatial distribution and interaction strength of the IX_1 (and thus earlier saturation), whereas the opposite trend applies to IX_2 .

With the established PSF mechanism, we can further understand the spectral redshifts observed in the MPB (Fig. 4f). By applying the saturation model to the hybridized anti-aligned IX_1 and IX_2 (Supplementary Note 6)^{13,43}, we approximate the expected energy shifts, which show qualitative agreement with our experimental results. Although precise quantification of the polariton nonlinearity warrants further investigation using higher-quality samples with more accurate measurements, this analysis suggests that the MPB nonlinearity arises from the synergistic interplay of the composite anti-aligned dipolar excitons.

Conclusion

In this work, we demonstrate electrically programmable strong coupling and distinct nonlinear interactions of dipolar polaritons with tunable IX hybridization in a 2L-MoS₂–1DPC system. The tightly confined photonic mode enables strong coupling to bright dipolar excitons under the influence of the QCSE within a single planar architecture. Utilizing the electrically compatible grating geometry, we apply a vertical electrostatic field across the 2L-MoS₂ to lift the IX degeneracy and Stark-tune the anti-aligned dipolar excitons, thereby continuously reconfiguring the polariton composition. As the split IX₁ and IX₂ emerge, they hybridize with the cavity photon to form an emergent MPB, characterized by non-monotonic Stark shifts with electrically addressable anti-aligned dipolar configurations. Crucially, the applied field serves as an *in situ* control knob to program the dipolar configurations, exciton hybridization, and consequently the nonlinear response of the polaritons. Looking forward, integrating this tunable platform with moiré superlattices may enable flat-band and topological polariton engineering, while further enhancing photon confinement could drive the system toward the polariton-blockade^{49,50} regime for scalable quantum photonic devices.

Methods

Sample preparation

Si₃N₄ grating with integrated electrodes. The Si₃N₄ film was first evaporated via PECVD on a pre-clean silica substrate, followed by electron beam lithography and reactive ion etching to obtain the grating structure. The grating was characterized by scanning electron microscope and angle-resolved reflection spectra, and the applicable gratings were adopted for optical lithography to fabricate the electrodes.

TMD heterostructures. The heterostructure was constructed from mechanically exfoliated 2H-stacked bilayer MoS₂, hBN, and graphene flakes. The bilayer MoS₂ was first identified by optical microscopy and further confirmed by photoluminescence spectroscopy, as well as its characteristic reflectance. Few-layer hBN and graphene flakes were prepared using the same exfoliation method. To minimize optical absorption and cavity loss, the graphene was chosen as thin as possible. The stack was assembled in a graphene/hBN/bilayer MoS₂/hBN/graphene sequence using a PDMS/polycarbonate film-based dry-transfer process, and then transferred onto the pre-fabricated grating with pre-patterned electrodes, with the graphene gates precisely aligned to the contacts. Finally, the device was annealed at 200 °C for 2h under a nitrogen atmosphere to improve interfacial flatness and remove residual organics.

Optical Characterization

All optical experiments were performed at 6 K in a Montana cryostat. The optical setup was a home-built Fourier-imaging microscope capable of switching between real-space and momentum-space measurements. Excitation and collection were both realized using a 50× objective (NA = 0.5) integrated into an Olympus microscope. All signals were dispersed by a spectrometer (Princeton Instruments, 600 lines/mm grating) and detected by a charge-coupled device.

For steady-state reflection spectroscopy, a broadband halogen lamp was used as the light source. For nonlinear optical experiments, a broadband supercontinuum white-light source was generated by focusing a narrowband femtosecond laser (50 kHz repetition rate, 222 fs pulse duration) onto a sapphire crystal. The bias voltage was applied using a source meter.

Simulation

All the simulation results were obtained based on COMSOL Multiphysics 6.3. We set the material parameters that are consistent with the experiments. These parameters include the refractive index of silicon nitride, the structure geometry parameters of the grating, the refractive indices, and the actual thicknesses of each layer in the hybrid

vdW heterostructure of hBN-encapsulated 2L-MoS₂.

Acknowledgments

This work was supported by the National Key Research and Development Program of China (No. 2021YFA1200800), the National Natural Science Foundation of China (Grant Nos. 12304429, 62261160386), and the Open Research Fund of the Pulsed High Magnetic Field Facility (Grant No. WHMFC2024015), Huazhong University of Science and Technology.

We thank Dr. Xinyuan Zhang from the Core Facility of Wuhan University for her assistance with AFM (atomic force microscope) test.

Author contributions

X.L. Q.G, and H.K. conceived and designed the project. H.K. carried out all optical spectroscopy measurements and characterized the devices, and prepared the samples with assistance from T.Z., W.D. and Q.G. H.K. analyzed the data with input from X.L. and Q.G. T.T. and K.W. provided high-quality hBN crystals. F.S., T.Y. and H.X. provided important guidance on manuscript preparation. All authors contributed to the paper. All work was supervised by X.L., Q.G., and T.Y.

Conflict of interest

The authors have no conflicts to disclose.

References

1. Lodahl, P., Mahmoodian, S. & Stobbe, S. Interfacing single photons and single quantum dots with photonic nanostructures. *Rev. Mod. Phys.* **87**, 347–400 (2015).
2. Deng, H., Haug, H. & Yamamoto, Y. Exciton-polariton Bose-Einstein condensation. *Rev. Mod. Phys.* **82**, 1489–1537 (2010).
3. Sanvitto, D. & Kéna-Cohen, S. The road towards polaritonic devices. *Nat. Mater.* **15**, 1061–1073 (2016).
4. Ghosh, S. *et al.* Microcavity exciton polaritons at room temperature. *Photon. Insights* **1**, R04 (2022).
5. Bloch, J., Cavalleri, A., Galitski, V., Hafezi, M. & Rubio, A. Strongly correlated electron-photon systems. *Nature* **606**, 41–48 (2022).
6. Luo, S., Zhou, H., Zhang, L. & Chen, Z. Nanophotonics of microcavity exciton-polaritons. *Appl. Phys. Rev.* **10**, 011316 (2023).
7. Kasprzak, J. *et al.* Bose-Einstein condensation of exciton polaritons. *Nature* **443**, 409–414 (2006).
8. Amo, A. *et al.* Superfluidity of polaritons in semiconductor microcavities. *Nat. Phys.* **5**, 805–810 (2009).
9. Christopoulos, S. *et al.* Room-Temperature Polariton Lasing in Semiconductor Microcavities. *Phys. Rev. Lett.* **98**, 126405 (2007).
10. Bhattacharya, P., Xiao, B., Das, A., Bhowmick, S. & Heo, J. Solid State Electrically Injected Exciton-Polariton Laser. *Phys. Rev. Lett.* **110**, 206403 (2013).
11. Schneider, C. *et al.* An electrically pumped polariton laser. *Nature* **497**, 348–352 (2013).
12. Li, H. *et al.* All-optical temporal logic gates in localized exciton polaritons. *Nat. Photon.* **18**, 864–869 (2024).
13. Zhao, J. *et al.* Room temperature polariton spin switches based on Van der Waals superlattices. *Nat. Commun.* **15**, 7601 (2024).
14. Berloff, N. G. *et al.* Realizing the classical XY Hamiltonian in polariton simulators. *Nat. Mater.* **16**, 1120–1126 (2017).
15. Tao, R. *et al.* Halide perovskites enable polaritonic XY spin Hamiltonian at room temperature. *Nat. Mater.* **21**, 761–766 (2022).
16. Zhang, L. *et al.* Van der Waals heterostructure polaritons with moiré-induced nonlinearity. *Nature* **591**, 61–65 (2021).
17. Gu, J. *et al.* Enhanced nonlinear interaction of polaritons via excitonic Rydberg states in monolayer WSe₂. *Nat. Commun.* **12**, 2269 (2021).
18. Emmanuele, R. P. A. *et al.* Highly nonlinear trion-polaritons in a monolayer semiconductor. *Nat. Commun.* **11**, 3589 (2020).
19. Wei, K. *et al.* Charged biexciton polaritons sustaining strong nonlinearity in 2D semiconductor-based nanocavities. *Nat. Commun.* **14**, 5310 (2023).
20. Luo, Y. *et al.* Manipulating nonlinear exciton polaritons in an atomically-thin semiconductor with artificial potential landscapes. *Light Sci. Appl.* **12**, 220 (2023).
21. Khestanova, E. *et al.* Electrostatic Control of Nonlinear Photonic-Crystal Polaritons in a Monolayer Semiconductor. *Nano Lett.* (2024).
22. Cristofolini, P. *et al.* Coupling Quantum Tunneling with Cavity Photons. *Science* **336**, 704–707

(2012).

23. Togan, E., Lim, H.-T., Faelt, S., Wegscheider, W. & Imamoglu, A. Enhanced Interactions between Dipolar Polaritons. *Phys. Rev. Lett.* **121**, 227402 (2018).
24. Rosenberg, I. *et al.* Strongly interacting dipolar-polaritons. *Sci. Adv.* **4**, eaat8880 (2018).
25. Jauregui, L. A. *et al.* Electrical control of interlayer exciton dynamics in atomically thin heterostructures. *Science* **366**, 870–875 (2019).
26. Wilson, N. P., Yao, W., Shan, J. & Xu, X. Excitons and emergent quantum phenomena in stacked 2D semiconductors. *Nature* **599**, 383–392 (2021).
27. Barré, E. *et al.* Optical absorption of interlayer excitons in transition-metal dichalcogenide heterostructures. *Science* **376**, 406–410 (2022).
28. Huang, D., Choi, J., Shih, C.-K. & Li, X. Excitons in semiconductor moiré superlattices. *Nat. Nanotechnol.* **17**, 227–238 (2022).
29. Du, L. *et al.* Moiré photonics and optoelectronics. *Science* **379**, eadg0014 (2023).
30. Huang, S. *et al.* Bright dipolar excitons in twisted black phosphorus homostructures. *Science* **386**, 526–531 (2024).
31. Unuchek, D. *et al.* Room-temperature electrical control of exciton flux in a van der Waals heterostructure. *Nature* **560**, 340–344 (2018).
32. Unuchek, D. *et al.* Valley-polarized exciton currents in a van der Waals heterostructure. *Nat. Nanotechnol.* **14**, 1104–1109 (2019).
33. Sun, Z. *et al.* Excitonic transport driven by repulsive dipolar interaction in a van der Waals heterostructure. *Nat. Photon.* **16**, 79–85 (2022).
34. Zhu, J., Liang, T., Shen, F., Chen, Z. & Xu, J. Observation of giant dipole moments of interlayer excitons via layer engineering. *Nat. Commun.* **16**, 10661 (2025).
35. Gerber, I. C. *et al.* Interlayer excitons in bilayer MoS₂ with strong oscillator strength up to room temperature. *Phys. Rev. B* **99**, 035443 (2019).
36. Leisgang, N. *et al.* Giant Stark splitting of an exciton in bilayer MoS₂. *Nat. Nanotechnol.* **15**, 901–907 (2020).
37. Peimyoo, N. *et al.* Electrical tuning of optically active interlayer excitons in bilayer MoS₂. *Nat. Nanotechnol.* **16**, 888–893 (2021).
38. Liu, X. *et al.* Optical signatures of interlayer electron coherence in a bilayer semiconductor. *Nat. Phys.* **21**, 1563–1569 (2025).
39. Tang, Y. *et al.* Tuning layer-hybridized moiré excitons by the quantum-confined Stark effect. *Nat. Nanotechnol.* **16**, 52–57 (2021).
40. Lopriore, E. *et al.* Electrically tunable ultrafast dynamics and interactions of hybrid excitons in a 2D semiconductor bilayer. *Nat. Commun.* **16**, 10710 (2025).
41. Feng, S. *et al.* Highly tunable ground and excited state excitonic dipoles in multilayer 2H-MoSe₂. *Nat. Commun.* **15**, 4377 (2024).
42. Feng, S. *et al.* Quadrupolar and Dipolar Excitons in Bilayer 2 H – MoSe₂. *Phys. Rev. Lett.* **134**, 166901 (2025).
43. Datta, B. *et al.* Highly nonlinear dipolar exciton-polaritons in bilayer MoS₂. *Nat. Commun.* **13**, 6341 (2022).
44. Louca, C. *et al.* Interspecies exciton interactions lead to enhanced nonlinearity of dipolar excitons and polaritons in MoS₂ homobilayers. *Nat. Commun.* **14**, 3818 (2023).
45. Genco, A. *et al.* Femtosecond switching of strong light-matter interactions in microcavities

with two-dimensional semiconductors. *Nat. Commun.* **16**, 6490 (2025).

- 46. Meng, Y. *et al.* Strong-interaction-driven quadrupolar-to-dipolar exciton transitions in a trilayer moiré superlattice. *Nat. Photon.* **19**, 1219 (2025).
- 47. Kravtsov, V. *et al.* Nonlinear polaritons in a monolayer semiconductor coupled to optical bound states in the continuum. *Light Sci. Appl.* **9**, 56 (2020).
- 48. Zhao, Y. *et al.* Interlayer exciton complexes in bilayer MoS₂. *Phys. Rev. B* **105**, L041411 (2022).
- 49. Liran, D. *et al.* Electrically Controlled Photonic Circuits of Field-Induced Dipolaritons with Huge Nonlinearities. *Phys. Rev. X* **14**, 031022 (2024).
- 50. Delteil, A. *et al.* Towards polariton blockade of confined exciton–polaritons. *Nat. Mater.* **18**, 219–222 (2019).